



# Analysis of intracellular protein dynamics in living zebrafish embryos using light-sheet fluorescence single-molecule microscopy

MATTEO BERNARDELLO,<sup>1,5</sup> RADOSLAW J. GORA,<sup>2,5</sup> PATRICK VAN HAGE,<sup>2</sup>  GUSTAVO CASTRO-OLVERA,<sup>1</sup>  EMILIO J. GUALDA,<sup>1</sup> MARCEL J. M. SCHAAF,<sup>2,3,6</sup> AND PABLO LOZA-ALVAREZ<sup>1,4,6</sup> 

<sup>1</sup>*ICFO-Institut de Ciències Fotoniques, The Barcelona Institute of Science and Technology, Castelldefels, 08860, Spain*

<sup>2</sup>*Institute of Biology, Leiden University, Leiden, The Netherlands*

<sup>3</sup>*m.j.m.schaaf@biology.leidenuniv.nl*

<sup>4</sup>*pablo.loza@icfo.eu*

<sup>5</sup>*Equal contribution*

<sup>6</sup>*Equal contribution*

**Abstract:** Single-molecule microscopy techniques have emerged as useful tools to image individual molecules and analyze their dynamics inside cells, but their application has mostly been restricted to cell cultures. Here, a light-sheet fluorescence microscopy setup is presented for imaging individual proteins inside living zebrafish embryos. The optical configuration makes this design accessible to many laboratories and a dedicated sample-mounting system ensures sample viability and mounting flexibility. Using this setup, we have analyzed the dynamics of individual glucocorticoid receptors, which demonstrates that this approach creates multiple possibilities for the analysis of intracellular protein dynamics in intact living organisms.

© 2021 Optical Society of America under the terms of the [OSA Open Access Publishing Agreement](#)

## 1. Introduction

A quantitative imaging-based analysis of the biochemical processes and protein interactions inside cells requires microscopy techniques that go beyond ensemble averaging and a static molecular view [1]. Single-molecule microscopy (SMM) has demonstrated to offer such opportunities and has enabled researchers to detect individual molecules in the variety of their conformations and associations as well as to study their dynamics with unparalleled spatial and temporal resolution. Imaging of individual proteins in living cells is enabled by fluorescent labeling of these proteins, using either genetically encoded fusion to autofluorescent proteins such as green fluorescent protein (GFP) and photoactivatable or switchable variants of these proteins, or linking of nanoparticles or organic dyes to peptide or protein tags (such as Halo-tags), that have been fused to the protein of interest [2–5].

SMM has mainly been performed using microscopy techniques such as Widefield Microscopy (WM), Total Internal Reflection Fluorescence (TIRF) microscopy, and Highly-Inclined and Laminated Optical sheet (HILO). In WM, while technically simple, the entire sample is illuminated by the excitation beam, which creates a high background over the weak signal from the single molecules. In TIRF, an evanescent wave of excitation light at the coverslip-sample interface is created, which exponentially decays with the distance to this interface [6]. As a result, only the fluorophores present in the first 100 to 200 nm are excited, which highly reduces the background intensity, and thereby increases the sensitivity and positional accuracy. However, at the same time, TIRF limits the detection of molecules to the basal membrane of the cells mounted on the coverslip. In HILO microscopy an oblique sheet of light is used to illuminate a section of the specimen, enabling excitation of fluorophores deeper inside cells [7]. Nevertheless, since

the illumination is oblique with respect to the detection focal plane, the size of the lateral Field-of-View (FoV) of the produced images is limited. Moreover, all these approaches are optimized for, and therefore limited to, coverslip-based sample mounting.

Thus far, the vast majority of SMM studies have been performed in cultured eukaryotic cells, often derived from immortalized cell lines. These cells may show artefacts, do not take into consideration the influence of cell-cell interactions, and have a limited translational value compared to studies performed in intact organisms. In addition, studies in cultured cells cannot answer questions concerning differences in protein dynamics in response to different developmental, environmental, and metabolic states that an organism might be presented with in its native habitat. Therefore, there is a need for microscopy techniques that enable *in vivo* SMM analyses on biologically relevant samples, such as the living zebrafish. These techniques should provide limited background signals and large FoVs, enable maintaining the sample alive for prolonged times, and, ideally, not interfere with natural biological processes by limiting phototoxic effects or other stressors. Previously, we have extended SMM studies to living organisms by analyzing the dynamics of yellow fluorescent protein (YFP) fused to the membrane anchor of the human H-Ras protein in cells inside living zebrafish embryos [8]. By using TIRF microscopy and a particular sample-mounting procedure to make the zebrafish tail adhere to the coverslip, we managed to detect individual YFP-C10H-Ras molecules in the outer membrane of the outer epithelial cells of the embryonic epidermis, and to study the mobility pattern of these proteins. However, while optimal for studies on membrane protein dynamics, the implementation of the TIRF microscopy is limited by the penetration depth of the evanescent wave and is therefore not suitable for studying molecules located anywhere outside the outer membrane of the outer cell layer of the embryo. In the present study, we have applied Light-Sheet Fluorescence Microscopy (LSFM) as an SMM technique that allows for imaging of individual non-membrane molecules inside a living organism while not being limited to the cell membrane.

In LSFM, two objectives, positioned orthogonally to each other, are usually employed. A plane of excitation light (light sheet, LS) is sent from the illumination objective through the specimen, exciting only the fluorophores present at the detection focal plane [9]. Photons emitted by the fluorophores in the entire illuminated sample section are collected in a widefield configuration by the detection objective. This plane-based configuration permits fast imaging and allows for optical sectioning at low photobleaching and phototoxicity regimes, with low background fluorescent signals.

The use of LSFM in SMM applications has so far been limited, mainly due to mechanical constraints imposed by the geometry of the objectives. Their orthogonality combined with their short working distances restricts the space and displacement possibilities of the sample. This problem has often been circumvented by the use of long-working-distance air objectives for the illumination, and cuvettes containing imaging medium and sample [10–13]. This solution, however, introduces refractive index mismatches at the air-glass and glass-medium interfaces, leading to spherical aberrations. Consequently, when the cuvette translates in the illumination direction, focal shifts appear and correction strategies need to be implemented [11], increasing hardware complexity. To overcome these issues, some LSFM configurations use a modified light path, including prism-based LSFM (PCLSM) [14], and reflected LSFM (RLSFM) [15–17]. With these LSFM approaches individual, fluorescently labelled molecules have been imaged in aqueous solutions [10,12], cell nuclei of salivary glands extracted from *C. tentans* larvae [11,13], and membranes or nuclei of cultured cells [14,15]. Interestingly, these technologies also allowed imaging of individual injected Dextran-Alexa647 molecules in *Drosophila* [16], and transcription factors in zebrafish embryos [17]. Custom-made illumination objectives combined with non-Gaussian excitation schemes, such as Bessel plane illumination [18] and lattice LSFM (LLSFM) [19], have been used to create a long and thin LS. These techniques have been employed in SMM studies in embryonic stem cells [20,21], membrane dynamics in cultured cells and in

cells of the zebrafish eye [22], and living *Drosophila* [23,24]. The Light Sheet Fluorescence Single-Molecule Microscopy (LSFSMM) methods described above offer the possibility to use very high NA (from 1.0 to 1.4) detection objectives, but this is only possible at the expense of a highly increased hardware complexity of the overall system, which will limit the use of LSFSMM.

So far, single-molecule imaging has only been applied to intact living organisms in a few studies [8,17,23], which could be due to the difficulty for many biological labs in accessing the complex setups that are required. The described hardware complexity also has consequences for the sample mounting systems. In PCLSM [14], the sample is placed on a glass bottom dish over an inclined surface. Similarly, RLSFM [15,16] and LLSFM have been used for SMM in living zebrafish embryos [17,22], and in these studies the embryos were mounted on a glass bottom dish or glass coverslip and embedded in low melting agarose. In all these methods, the sample's degrees of freedom are constrained by the mounting procedure, as the specimen's movements and orientation possibilities are fixed or limited. Although this might not be a problem for cultured cells, in the case of imaging living organisms it can eventually preclude the performance of certain experiments.

In the present study, we chose an iSPIM [25] configuration to perform SMM, to have a simpler setup compared to the previously mentioned LRFM alternatives, without custom-made optical elements such as coatings [15,17] or objectives [19], thereby avoiding potential instability issues and maintaining a straightforward optical alignment procedure. Although the collection NA achieved in our system is smaller or equal compared to the NA of PCLSM, RLSFM, or LLSFM setups, our sample mounting approach is superior in terms of sample viability and sample mounting flexibility. We believe that these are crucial factors when extending the application of SMM to intact living organisms. In addition, our design will enable the possibility to perform more complex SMM studies *in vivo*, e.g. correlating macro-biological events with the intracellular dynamics at the single molecule level. We therefore describe the sample mounting procedure in detail, with attention to the effects of the embedding medium on the microscope's performance.

We have utilized our LSFSMM setup using cultured cells and living zebrafish embryos as biological samples. HEK293 cells were used to perform a characterization study on the detection of single yellow fluorescent protein (YFP) molecules. Subsequently, we chose zebrafish embryos to test our capacity to image *in vivo*, since it is a relevant vertebrate animal model that is commonly used in research areas, ranging from developmental biology to toxicology and drug screening [26,27]. As a protein of interest, we selected the Glucocorticoid Receptor (GR), which is a well-studied steroid receptor. Upon binding of a glucocorticoid ligand (either an endogenous hormone such as cortisol or a synthetic drug such as dexamethasone), the GR translocates to the nucleus and acts as a transcription factor, regulating gene expression by binding to specific DNA sequences and interacting with other proteins. Previous studies have allowed researchers to study the intranuclear dynamics of individual fluorescently tagged GR molecules in cultured cells and, for instance, establish the duration of the DNA binding time [15,28–31]. Furthermore, it has been exhibited that the zebrafish GR gene shows a high level of similarity with its human counterpart, through the similarity of a C-terminal GR splice variant, resembling the human GR $\beta$ , and the fact that both zebrafish and human genomes contain only one gene encoding the GR protein [32].

By using our custom-made and optimized mounting system in our LSFSMM, we demonstrate that it is possible to successfully image individual molecules in living embryos for a prolonged period of time. To validate the robustness of our LSFSMM, we have analyzed the GR mobility pattern. As expected, dexamethasone administration significantly alters the dynamics of GR. By further characterization of the sources of variation in the *in vivo* results, we found that most of the variability in the results comes from imaging different areas within an individual zebrafish embryo, and to a lesser extent from imaging individual embryos on different experimental days, discarding the microscope setup as a source of variation. Overall, our data suggest that the

relative simplicity of the optical design, constructed with conventional optical elements together with the described sample mounting system and protocols, will further promote *in vivo* LSFSMM applications in membranes, cytoplasm, and nuclei of cells inside zebrafish and other living organisms.

## 2. Methods

### 2.1. Zebrafish

Zebrafish (*Danio rerio*) were grown, maintained and handled in compliance with the directives of the local animal welfare body. They were exposed to a 14 h light and 10 h dark diurnal cycle at 28°C. Fertilization was performed by natural spawning at the beginning of the light period, and the fertilized eggs were collected and maintained in E3 medium (5 mM NaCl, 0.17 mM KCl, 0.33 mM CaCl<sub>2</sub>, 0.33 mM MgSO<sub>4</sub>) at 28°C. All experiments were performed using embryos from the *Tg(actb2:mCherry-H2A)* zebrafish line.

### 2.2. Microinjection and treatment of embryos

A cDNA construct encoding eYFP-GR(alpha), hereafter referred to as YFP-GR, was genetically cloned into a PCS2+ zebrafish expression plasmid. The resulting PCS2+-eYFP-GR(alpha) plasmid was microinjected into zebrafish embryos at the 1-2 cell stage (30 pg per embryo), resulting in a mosaic expression of the eYFP-GR(alpha) protein in the zebrafish embryo. Microinjections were done under a stereomicroscope (Leica S8AP0), using a microinjector (Pneumatic Pico Pump PV820, WPI) and a micromanipulator with pulled microcapillary pipettes (model GC100F-15 from Harvard Apparatus, pulled with P-97 Micropipette Puller from Sutter Instrument). Injected eggs were left to develop in an incubator at 28°C. Viability and development of the eggs after microinjections were checked on a daily basis using a fluorescence stereomicroscope (Nikon SMZ1000 C-DSD230). To prevent embryonic pigmentation, embryos were incubated in 0.003% phenylthiourea (PTU) from 10 hpf (hours post-fertilization) onwards, and this solution was refreshed daily. For treatment with the synthetic glucocorticoid dexamethasone, a 10 mM stock solution in DMSO was prepared. The zebrafish embryos were incubated in dexamethasone (final concentration of 25 μM) in egg water for 3 hours, at 28°C, prior to the microscopy imaging. As a control, a group of zebrafish embryos was incubated in a vehicle solution of 0.01% DMSO.

### 2.3. LSFSMM setup details

In the LSFSMM setup, the light from an ArKr laser (Innova 70C Spectrum, Coherent) is first passed through an acousto-optic tunable filter (AOTF<sub>NC</sub>-400.650-TN, AAOptoelectronics) to select the needed illumination wavelengths (514.5 nm for the YFP, and 568.2 nm for the mCherry molecules). After the AOTF (see Fig. 1(A)), the light beam is sent to a telescope (AC254-030-A-ML, AC254-250-A-ML, Thorlabs), going through a spatial filter (with a 30 μm pinhole) to produce a clean Gaussian beam. The collimated beam is then focused by a cylindrical lens (focal length of 75 mm, LJ1703RM-A, Thorlabs). An additional telescope (AC254-100-A-ML, AC254-200-A-ML, Thorlabs) is then used to illuminate the back-focal plane (BFP) aperture of a water immersion illumination objective (10X Nikon CFI Plan Fluorite Objective, 0.30 NA, 3.5 mm working distance (WD)) that will finally project the light sheet at the sample plane. The illumination path also incorporates, in a conjugated plane with the BFP of the illumination objective, a galvanometric mirror (GVS002, Thorlabs) that allows scanning the light sheet across the sample volume. In the detection path, the fluorescent signal is collected by a water-dipping detection objective (20X Olympus XLUMPLFLN Objective, 1.00 NA, 2.0 mm WD). This is passed through a motorized filter wheel (FW103H, Thorlabs) and a 200 mm tube lens (TTL200-A, Thorlabs). A periscope formed by an additional telescope (TTL100-A and TTL200-A, Thorlabs) permits an additional 2× magnification and projects the image onto the chip of a sCMOS camera

(OrcaFlash4 v.3, Hamamatsu). With this configuration (Olympus objective coupled to 200 mm tube lens and 2x periscope), the total magnification is 44.4x.

#### 2.4. Determination of imaging parameters

To measure the thickness of the light sheet, the cylindrical lens was removed from the optical path, and the beam that was focused through a fluorescent solution by the illumination objective was imaged. Using FIJI software [33], the intensity line profile at the beam waist was generated and Gaussian-fitted (Fig. 2(A)). The standard deviation  $\sigma$  of the Gaussian fit was used to calculate the full width at half maximum (FWHM) of the intensity line profile as  $FWHM = 2\sigma \cdot \sqrt{(2 \cdot \ln 2)} \approx 2.355\sigma$ , which represents the light sheet thickness waist diameter, and equaled  $2 \mu\text{m}$ . The illumination field of view (FoV) was calculated as in Olarte *et al.* [9], i.e.,  $FoV = 1.78 \cdot n \cdot \frac{\lambda}{(NA)^2}$ , where  $n$  is the medium refractive index (water),  $\lambda$  is the illumination wavelength, and  $NA$  is the illumination objective's numerical aperture, and equaled  $13.5 \mu\text{m}$ . The illumination FoV, considered as the double of the Rayleigh range, was also measured on the imaged beam profile and found to be  $14.5 \mu\text{m}$ , in good agreement with the theoretical value. To obtain the excitation power density, the optical losses introduced by the illumination path were first determined. These were about 69%, due to the overfilling of the back-focal plane of the objective, to ensure homogeneous illumination. By setting the power at the input port of the microscope at 66 mW, the power at the sample plane resulted in 20.25 mW. Being the illumination focal plane area defined by the thickness ( $2 \mu\text{m}$ ) and height (1.2 mm) of the light sheet, the resulting power density equaled  $\sim 0.85 \text{ kW cm}^{-2}$ . To measure the optical resolution of the system, sub-diffraction fluorescent beads (100 nm in diameter) were embedded in 0.5% low melting point agarose (lmpa) and placed as sample in the microscope using a Fluorinated Ethylene Propylene (FEP) support. Images were taken for beads close to the middle axis and near the surface of the produced agarose cylinder (Fig. 2(C) and Fig. 2(E) respectively). The intensity profiles in  $\hat{x}$  and  $\hat{y}$  were measured, Gaussian fitted, and their FWHMs calculated. Shapiro-Wilk tests were performed to confirm the normal distribution of the FWHMs values. Unpaired t-tests were then conducted to check for statistically significant difference between the values obtained for beads close to the middle axis (N=11 beads) and near the surface (N=11 beads), in both lateral directions (Fig. 2(B)).

#### 2.5. Cultured cells fixation, mounting, and LSFsMM imaging

To determine the characteristics of the detection of a single YFP molecule in the LSFsMM setup, HEK293 cells were transfected with the plasmid PCS2+-eYFP-GR(alpha) for expression of YFP-GR. For transfection, cells were cultured in DMEM (Dulbecco's Modified Eagle Medium, Invitrogen, Waltham, MA, USA) supplemented with penicillin and streptomycin ( $10 \mu\text{g ml}^{-1}$ , Invitrogen), Glutamax ( $10 \mu\text{g ml}^{-1}$ , Invitrogen) and 10% fetal calf serum (Invitrogen) at  $37^\circ\text{C}$  in humidified atmosphere containing 5% of  $\text{CO}_2$ . Before transfection, cells were transferred onto a sterile glass coverslip (diameter 25 mm, Marienfeld, Germany) and placed in a well of a 6-well plate. At a confluence level of 20-30%, cells were transfected with  $1 \mu\text{g}$  of DNA per well, using FuGENE 6 (Roche Molecular Biochemicals, Indianapolis, USA). The transfection efficiency, determined by fluorescence microscopy screening at 48 h after transfection, was approximately 20%. Two days post-transfection cells were fixed with 4% PFA. Fixed cells were then immersed in 0.5% lmpa, transferred into a cut FEP support tube, and mounted in the LSFsMM system. Movies were taken using continuous illumination and a 25 ms exposure time per frame for 1000-4000 frames.

### 2.6. Determination of the fluorescence signals characteristics derived from individual YFP molecules

To determine the characteristics of the fluorescence signals derived from individual YFP molecules, as detected using our setup, we imaged fixed transfected HEK293 cells (3 days post-transfection). For this purpose, a two-dimensional Gaussian curve was fitted over all the fluorescence intensity spots found in the images of a fixed HEK293 cell. Subsequently, the maximal value and the full width at half maximum (FWHM) of the fitted Gaussian curves were determined in order to establish threshold values for the proper identification of intensity spots reflecting single molecules [2]. Tracking of the identified intensity spots using custom software [34] showed single-step photobleaching for all spots, confirming that they could be attributed to individual YFP molecules.

### 2.7. Live zebrafish embryo mounting and LSFMM imaging

A cut FEP tube was mounted through a glass capillary inside the incubation chamber. Impa solutions (2% and 0.5% in E3 medium) were heated up to 70°C, and 2% Impa was applied to the distal and proximal ends of the cut tube as well as at the basis (see Fig. 1) and left to solidify. Naturally hatched zebrafish embryos were transferred to a petri dish containing E3 medium with tricaine (100 mg L<sup>-1</sup>). Subsequently, an embryo was transferred to a glass bottom petri dish, the E3 medium was removed, and 0.5% Impa (cooled down, with 100 mg L<sup>-1</sup> tricaine) was poured onto the glass petri dish. While still liquid, a drop of 0.5% Impa, together with the zebrafish embryo, was aspirated through a glass pipette and carefully transferred into the FEP support, on top of the already present 2% Impa layer. The incubation chamber with the FEP tube containing the zebrafish embryo was mounted into the setup, on top of a platform connected to a xyz motorized stage (8MTF from Standa for xy-translations, 8302 Picomotor Actuator from Newport, connected to LX10/M from Thorlabs, for z-translations). The glass capillary was connected, using a screw, to a stepper motor (L4018S1204-M6, Nanotec) for sample rotation. E3 medium with tricaine (100 mg L<sup>-1</sup>) was poured into the imaging chamber at room temperature, to completely immerse the sample and the tip of the objectives. Using a custom-made software in LabVIEW, the position of the sample in x, y, and z was adjusted to be in the FoV of the detection objective. Rotation around the y-axis of the specimen and the movement in z of the light sheet provided additional alignment flexibility and possibilities to change the imaged area. The position of the detection objective was manually adjusted. A region of interest (ROI) was selected based on the mCherry signal (from the nuclear mCherry-H2A protein, illumination wavelength 568.2 nm, emission filter FF01-620/14-25, Semrock) to localize the nuclei. The YFP signal (from the YFP-GR protein, illumination wavelength 514.5 nm, emission filter FF01-535/22-25, Semrock) was chosen to confirm the expression of the fluorescently labeled GR. Once a ROI was selected, a movie of the YFP signal was recorded using continuous illumination and a 25 ms exposure time per frame for 1000-4000 frames. The PTU treatment prevented the pigmentation of the sample, i.e. avoiding light-sheet shadowing effects. In case a shadowing effect would have occurred, the region of interest could have been changed through sample translation/rotation.

### 2.8. Live imaging using the muviSPIM setup

To check the presence and localization of GR in the zebrafish embryos, lower resolution imaging was performed. A PTU-treated, non-dechorionated 1 dpf (day post-fertilization) embryo was embedded in a 1.5% Impa cylinder and immersed in the incubation chamber of a custom-made LSFMM setup in the muviSPIM configuration [35]. The incubation chamber was filled with E3 medium with tricaine (400 mg L<sup>-1</sup>) and its temperature maintained at 26.5°C. Z-stack images were acquired of the embryos for both the YFP and mCherry signals every 15 minutes during 22 hours. A sequential illumination scheme was employed to illuminate both sides of the embryo. Light sheets (at 488 nm for YFP excitation and at 561 nm for mCherry excitation) were generated

through the coupling of cylindrical lenses (LJ1703RM-A, Thorlabs, focal length 75 mm) and air objectives (4X Nikon Plan Fluorite Imaging Objective, 0.13 NA, 17.2 mm WD). The emitted photons were collected through a 10X Nikon CFI Plan Fluorite Objective (0.30 NA, 3.5 mm WD) and a sCMOS camera (OrcaFlash4 v.2, Hamamatsu).

## 2.9. Data analysis

To study the mobility of proteins, Particle Image Correlation Spectroscopy (PICS) analysis was used, described in detail previously [36,37]. In PICS analysis, individual molecules are not tracked, but all possible correlations between the locations of molecules in two image frames are determined. This way, a cumulative distribution function of distances is generated, which includes both contributions from diffusing molecules as well as random correlations between unrelated molecules in the two frames. The latter follows a linear relation in the cumulative distribution plot and is subtracted prior to further analysis, yielding cumulative probability distributions of displacements  $r_i$  for each of the time lags, which are fitted to a one- or two-fractional model. The former is described by the equation:

$$P(r^2, t_{lag}) = 1 - \exp\left(-\frac{r^2}{r_0^2(t_{lag})}\right) \quad (1)$$

which assumes the probability of the molecule starting at the arbitrary origin can be found within a circle of a radius  $r$  at the time lag  $t_{lag}$ . Alternatively, in case the population of molecules could be divided into two subpopulations with different mobility, Eq. (1) was transformed into the equation:

$$P(r^2, t_{lag}) = 1 - \left[ \alpha \cdot \exp\left(-\frac{r^2}{r_1^2(t_{lag})}\right) + (1 - \alpha) \cdot \exp\left(-\frac{r^2}{r_2^2(t_{lag})}\right) \right] \quad (2)$$

where the displacements  $r$  of two subpopulations are denoted by  $r_1$  and  $r_2$ , and the relative size of these subpopulations by  $\alpha$  and  $(1 - \alpha)$ .

A multistep analysis was performed for each movie acquired, analyzing correlations over five different time lags (25, 50, 75, 100, and 125 ms). Due to photobleaching the number of displacements  $r^2$  becomes smaller with increasing time lag. Nonetheless, even for such higher time lags, a minimal number of displacements remains in the order of  $10^5$ , as the number of images per movie is large (1000-4000 images per movie). To examine the type of diffusion of these subpopulations of molecules, the values of  $r_1^2$  and  $r_2^2$  were plotted against the time lag. The positional accuracy ( $dx$ ) led to a constant offset in  $r_i^2$  of  $4 \cdot (dx)^2$ . In case this plot showed a linear relationship, a Brownian diffusion was assumed, and a curve was fitted with the equation:

$$r_i^2(t_{lag}) = 4 \cdot D \cdot t_{lag} \quad (3)$$

in which  $D$  is the diffusion coefficient. If the plot reached a plateau at larger time lags, a confined model was fitted with the Eq. (4):

$$r_i^2(t_{lag}) = \frac{L^2}{3} \cdot \left[ 1 - \exp\left(-\frac{12 \cdot D_0 \cdot t_{lag}}{L^2}\right) \right] \quad (4)$$

in which the molecules diffuse freely with an initial diffusion coefficient  $D_0$  and are confined to an area described by a square with a side length  $L$ .

## 2.10. Experimental design

On three experimental days, one zebrafish embryo was selected for the LSFSMM imaging per experimental (vehicle- and dexamethasone-treated) group, and in each of the selected embryos,

three separate areas were imaged, yielding three independent movies of 1000-4000 consecutive frames. All movies were analyzed individually, resulting in a value per movie for  $\alpha$ ,  $r_1^2$  and  $r_2^2$  for each time lag. In the analysis of the HEK293 cells, one cell was selected for single peak shape analysis and single-step photobleaching. The values of  $\alpha$ ,  $r_1^2$  and  $r_2^2$  were also determined in fixed HEK293 cell data for comparison (See [Supplement 1](#), Fig. S1, Table S1).

### 2.11. Statistical analysis

Statistical analysis was performed in R statistical software (R: a language and environment for statistical computing, <https://www.R-project.org>). Values of  $\alpha$  and  $r_1^2$  were compared between the two groups, vehicle- and dexamethasone-treated, pooling all the values from individual images from three experimental days. In order to check if data were normally distributed, a Shapiro-Wilk test was performed. Significance of the results was conducted using a mixed-effect model for comparison of means between two normally distributed groups.

A hierarchical linear model was used to estimate the variance components within a hierarchically nested sampling design, between embryos from each experimental day, different cell nuclei in a single embryo, and different images of the same nucleus in an individual embryo. The model also took into account the residual variability component, which accounts for the variability that cannot be explained by the parameters used in our experimental design. As a single, time lapse, image might contain up to 30 thousand trajectories of single molecules, correlation coefficients were calculated for the relationships between number of such trajectories and fast-diffusing fraction size,  $\alpha$ , as well as mean squared displacements of fast- and slow-diffusing fractions,  $r_1^2$  and  $r_2^2$ . Subsequently, sources of potential variability within the experimental design were estimated by using a linear mixed model with square root transformation of  $r_1^2$ , to ensure that the random errors follow a Gaussian distribution. Use of linear mixed models extends the applicability of a simple linear model, since the former incorporate both fixed and random effects. Random effects represent the special case of fixed effects that are nested within the data, and demonstrate a subject- or group-specific variation. Linear mixed models are commonly used to account for the data where measurements are made on clusters of related statistical units [38,39].

The fitting of the linear mixed model was performed in R package, *lme4* [38]. To evaluate the contribution of each variance component towards the total variability, caterpillar plots were plotted to report the estimated group intercepts and the associated 95% confidence intervals, as a measure of relative deviation from the global mean of the data (See [Supplement 1](#), Fig. S2). For instance, an average value of one experimental day contained measurements of the same parameter obtained in all the areas of an embryo within the same day, while the analogous average for a single area entailed only those measurements that were acquired during repetitive imaging of only one area within the embryo. Those values were then sorted from the ones deviating most negatively from the total average to the ones that deviated most positively. Sorted deviations of the values were ultimately juxtaposed, in order to assess which variance component constitutes the major source of the measurement error. The corresponding values of variance for each of the parameter measured together with residual variance were calculated and presented together with their percentage contribution towards the total data variability.

## 3. Results

### 3.1. LSFM platform for *in vivo* SMM imaging (LSFSMM)

In order to achieve *in vivo* SMM on whole live organisms we have designed and built a customized LSFM platform. We took into special consideration the development of sample mounting protocols adapted to the experimental requirements and sample needs. Finally, we have characterized its optical performance and its ability to conduct SMM experiments.



Our LSFMM implementation is built on a Nikon Eclipse body, on top of which two perpendicular objectives are mounted in iSPIM configuration [25]. Since the two objectives are positioned perpendicularly between each other, but at  $45^\circ$  respect to the optical table, we define the coordinate system  $xyz$  to be the reference for the optical table and motor stages, while the coordinate system  $\hat{x}\hat{y}\hat{z}$  is defined as the reference for the imaging planes, with  $\hat{x}\hat{y}\hat{z}$  being the clockwise rotation of  $45^\circ$  around the  $y$ -axis of  $xyz$ . A schematic overview of the illumination and detection light paths is depicted in Fig. 1(A). The light sheet plane is generated by a cylindrical lens that focuses the light onto a galvo-mirror. The mirror is positioned plane-conjugate with the back-focal-plane of a water dipping illumination objective by a relay lens system. This arrangement permits to change the position in  $\hat{z}$  (i.e. across the sample volume) of the light sheet by electronically controlling the angle of the galvo-mirror. This capability can be used for alignment purposes and to scan different sample areas. With this illumination system, we experimentally measured the LS thickness to be of about  $2\ \mu\text{m}$  at its waist (Fig. 2(A)). The illumination FoV along  $\hat{x}$ , i.e. the portion of the light sheet that is considered to be of homogeneous thickness, is calculated to be about  $13.5\ \mu\text{m}$ , in good agreement with the measured value of about  $14.5\ \mu\text{m}$  (Fig. 2(A)). The total magnification of the optical system is  $44.4\times$  (See Material and Methods section), leading to an image pixel size of  $146.4\ \text{nm}$ . Considering the size along the  $\hat{y}$  axis of the sCMOS chip of the camera (2048 pixels), this means that the system enables the imaging of an area of about  $13.5\ \mu\text{m} \times 300\ \mu\text{m}$ .

In order to enable imaging in zebrafish embryos, an appropriate sample mounting system is key and should allow both optical quality and sample wellness. In the iSPIM configuration, the two objectives offer a limited volume in which the sample can be inserted. The sample mounting system must allow simple insertion of a zebrafish embryo and provide conditions for the embryo to stay alive during the experiment, with as little stress imposed as possible. At the same time, the sample mounting system needs to avoid the introduction of unwanted optical aberrations. We have implemented and characterized a fully motorized sample mounting stage and efficient sample mounting protocols using tailored FEP tubes and multilayer agarose mounting, as depicted in Fig. 1(B)-(D). The developed sample mounting system makes use of a FEP tube which was cut to free the top part. In this way the tube serves as a horizontal support for the relatively big and heavy sample without covering it. Its proximal and distal tips and the basis of the tube are filled with 2% low melting point agarose (Impa). The zebrafish embryo is placed in the remaining space inside a drop of 0.5% Impa with the addition of tricaine for anaesthesia. The FEP tube is suspended inside a petri-dish-like chamber by a 12 cm glass capillary, which is inserted into the proximal end of the FEP tube. The glass capillary is connected to a motorized rotator motor on its other end, and optimal orientation of the zebrafish embryo with respect to the LS can be obtained by rotating the capillary using simple electronic control of the motor. Finally, the incubation chamber, which is on top of an  $x$ - $y$ - $z$  motorized translational stage is filled with E3 medium (with the addition of tricaine), to completely immerse the zebrafish embryo and the tips of the objectives.

To characterize the effect of the sample mounting protocol on the generated optical aberrations, a FEP tube filled with a 0.5% Impa cylinder, in which sub-diffraction sized fluorescent beads (100 nm in diameter) were embedded, was introduced in the imaging volume. The image of a 100 nm fluorescent bead would present a theoretical FWHM of 334 nm, given by the convolution of the Gaussian PSF generated by a 1.0 NA water-objective, with the step-size profile of the bead. The images obtained from beads inserted close to the middle axis of the Impa cylinder would instead heavily suffer from distortions, enlarging the total PSF and reducing the actual optical resolution (Fig. 2(C)-(D)). For beads at this location, we calculated FWHMs of  $567.6 \pm 59.2\ \text{nm}$  and  $536.5 \pm 65.3\ \text{nm}$  (average  $\pm$  standard deviation, in  $\hat{x}$  and  $\hat{y}$  direction respectively,  $N=11$  beads). In contrast, images from beads closer to the surface of the 0.5% Impa cylinder did not suffer from significant distortions (Fig. 2(E)-(F)). For beads at this location, we calculated FWHMs

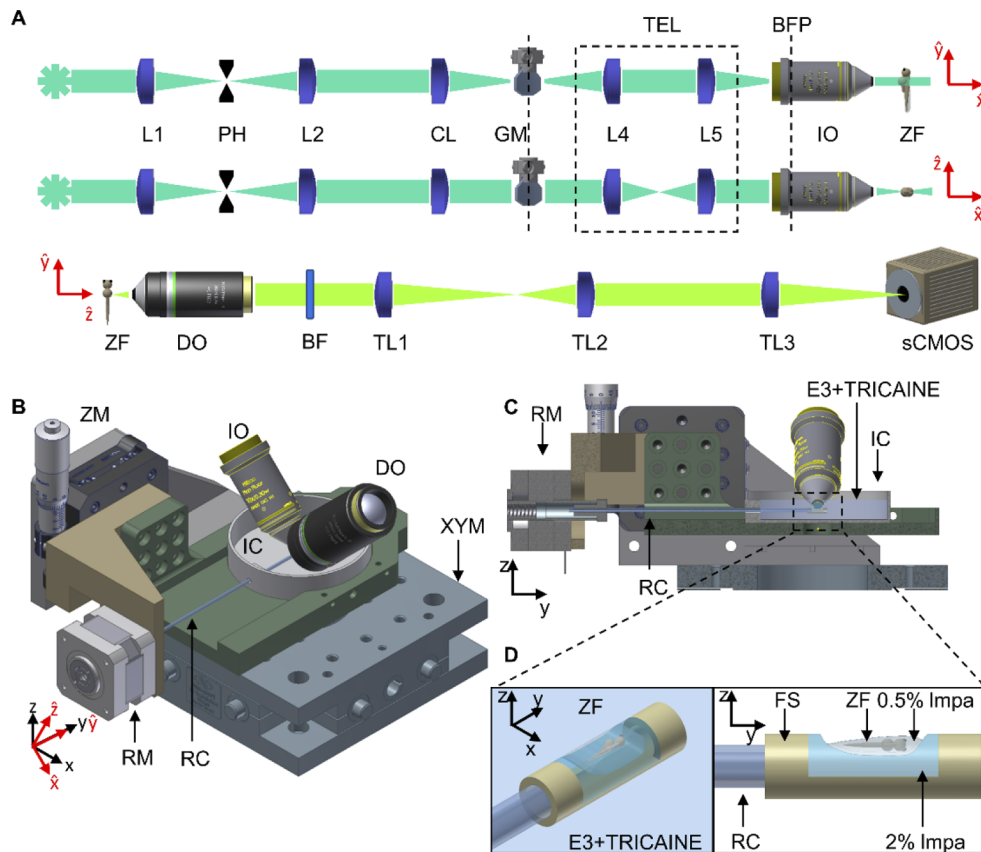


**Fig. 1.** Schematic overview of the LSMF platform for in vivo SMM imaging. (A) schematic of the optical illumination (top two) and detection (bottom one) light paths; (B) schematic of the sample mounting system, with (C) its lateral section view, (D) the FEP support for zebrafish mounting. L = lens, PH = pinhole, CL = cylindrical lens, GM = galvo-mirror, BFP = back focal plane, TEL = telescope plane-conjugating GM to BFP, IO = Illumination objective, DO = detection objective, BF = bandpass filter, TL = tube lens, ZF = zebrafish, RC = rotation capillary, FS = FEP support, RM = rotational motor, IC = imaging chamber, ZM = motorized stage in z, XYM = motorized stage in xy, Impa = low melting point agarose.

of  $393.0 \pm 39.9$  nm and  $371.4 \pm 34.8$  nm (average  $\pm$  standard deviation, in  $\hat{x}$  and  $\hat{y}$  direction respectively,  $N=11$  beads). The position of the point source within the Impa cylinder is therefore critical in assessing the optical resolution, which significantly differs for objects at the two locations (Fig. 2(B)).

The difference between the measured values from the beads close to the surface and the theoretical one is most probably imputable to a residual aberration caused by the remaining agarose layer, and thus depending on the exact position of the single beads. The system and protocol for mounting zebrafish embryos was therefore here developed such that the living specimen was covered by a maximally 100  $\mu\text{m}$ -thick layer of 0.5% Impa, in order to minimize optical aberrations.

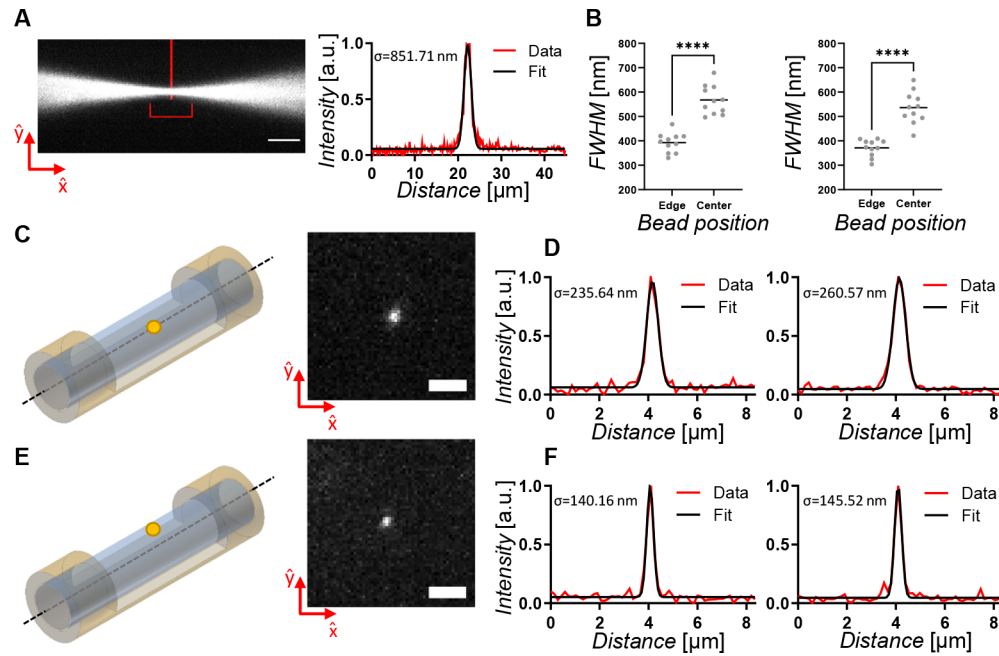


**Fig. 2.** LFSMMS system performances. (A) Illumination light beam focused by removal of the cylindrical lens. Measurement of the intensity profile through a Gaussian fit demonstrated a 2  $\mu\text{m}$  diameter (FWHM) at its waist (indicated by vertical red line). The illumination FoV is also indicated (red horizontal bracket). Scale bar 10  $\mu\text{m}$ . (B) Distributions and comparison of the measured FWHM of the Gaussian fits of beads close to the surface ( $N=11$ ) and in the center ( $N=11$ ) of the mounting Impa cylinder. Values were measured along  $\hat{x}$  (left panel) and  $\hat{y}$  (right panel) direction. Shapiro-Wilk test was performed to check if data is normally distributed. Unpaired t-tests were then conducted to check for statistically significant difference between the two conditions and calculate two-tailed P-values. Horizontal bar represents the mean value, \*\*\*\* means  $P < 0.0001$ . (C) Schematic of a 100 nm fluorescent bead positioned in the middle of a 0.5% Impa cylinder and (D) normalized intensity profile measurement and Gaussian fit in  $\hat{x}$  (left panel) and  $\hat{y}$  (right panel) direction of an imaged bead. Scale bar 2  $\mu\text{m}$ . (E) Schematic of a 100 nm fluorescent bead positioned close to the surface of a 0.5% Impa cylinder and (F) normalized intensity profile measurement and Gaussian fit in  $\hat{x}$  (left panel) and  $\hat{y}$  (right panel) direction of an imaged bead. Scale bar 2  $\mu\text{m}$ . For all the Gaussian fits here presented  $R^2 > 0.96$ , and  $\sigma$  represents the standard deviation of the Gaussian curve.

### 3.2. Characterization of detected fluorescence signals from individual YFP-GR molecules

The experiment was performed on HEK293 cells transiently transfected with an expression vector for YFP-GR. The cells were fixed to guarantee immobility of the fluorophores so they would not diffuse out of the FoV. Subsequently, the fixed cells were mounted on the LSFMM setup for imaging. Characteristics of the YFP molecule fluorescence signal (Fig. 3(A)), was determined by analysis of 1241 fluorescence intensity spots that displayed single-step photobleaching, which indicates the presence of a single fluorescent protein within a diffraction-limited spot. Almost 85% of all the single-molecule traces were 3 frames long or shorter, and the average trace length of a single YFP-GR molecule equaled 2.3 frames (Fig. 3(B)).

To extract the information about the point-spread function (PSF) of the fluorescence from a single YFP molecule, a Gaussian function was plotted over the 2D intensity profile (Fig. 3(A)). We determined the maximum of the Gaussian function as a measure for the intensity, while its full width at half maximum (FWHM) as a measure for the width of the PSF of a single YFP molecule. The maximum of the Gaussian function of 1241 signals from immobilized YFP-GR molecules in the fixed HEK293 cell equaled  $139.8 \pm 22.4$  counts, which corresponds to  $22.3 \pm 9.7$  photons (Fig. 3(C)). The mean FWHM value of the Gaussian curves fitted on the single-molecule intensity profiles equaled  $357.5 \pm 12.6$  nm. These characteristics of the fluorescence signals from individual YFP molecules were subsequently used to determine the threshold values for the identification of signals attributed to single YFP-GR molecules in the images acquired from living zebrafish embryos using previously developed, customized software [2,34,40] (Fig. 3(D)). The mean number of single YFP-GR molecules identified per image frame equaled  $19.6 \pm 8.7$ . The positional accuracy of the measurements was determined by calculating the quotient of the FWHM and square root of the number of photons detected, and equaled 76 nm [41], while Signal-to-Noise Ratio (SNR), being defined as the intensity of an individual fluorophore ( $139.8 \pm 22.4$  counts) divided by the standard deviation of the background signal (7.2 counts), equaled circa 20 (Fig. 3(C)).

### 3.3. Experiments on live fish and data analysis

In order to confirm the presence of the YFP-GR molecules and their localization within the nuclei of the embryonic cells, embryos of the *Tg(actb2:mCherry-H2A)* transgenic zebrafish line, which express a fusion protein of mCherry and the nuclear protein histone 2A in all cells, were injected with the YFP-GR expression vector and imaged at 1 dpf using a different custom-made LSFMM system setup. This multi-view LSFMM microscope allowed us to visualize, at 1.3  $\mu$ m lateral resolution and extended field of view, the development of the whole embryo [35]. The resulting images showed the expression of the YFP-GR molecules and their co-localization with the H2A histone signal (Fig. 4(A)-(C)) within the nuclei of the cells in the embryonic body. The YFP-GR expression was particularly evident in the external yolk syncytial nuclei (eYSN), which have migrated to cover the yolk sac during gastrulation. They are part of the yolk syncytial layer (YSL), a syncytium containing yolk syncytial nuclei (YSN) that is formed during early embryogenesis as a result of mitotic divisions without cytokinesis. It consists of internal YSN (iYSN, located between the yolk sac and the proper embryo) and eYSN that cover the yolk sac. The YSL plays an important role in meso- and endodermal differentiation, epiboly and cardiac formation, and it plays a nutritive role during embryonic and larval stages [42–45]. These giant nuclei are transcriptionally very active and have previously been shown to display high levels of transgene expression, which may be due to a high transcriptional activity or enhanced transgene replication in these nuclei [46]. We therefore chose these nuclei as target for our SMM intranuclear analysis, as upon DNA injection their expression levels are significantly higher than those of somatic nuclei.

Subsequently, using the LSFMM system high-resolution image sequences of the YFP-GR in the embryos were acquired with a time lag of 25 ms and a length of 1000-4000 frames (Fig. 4(D)).

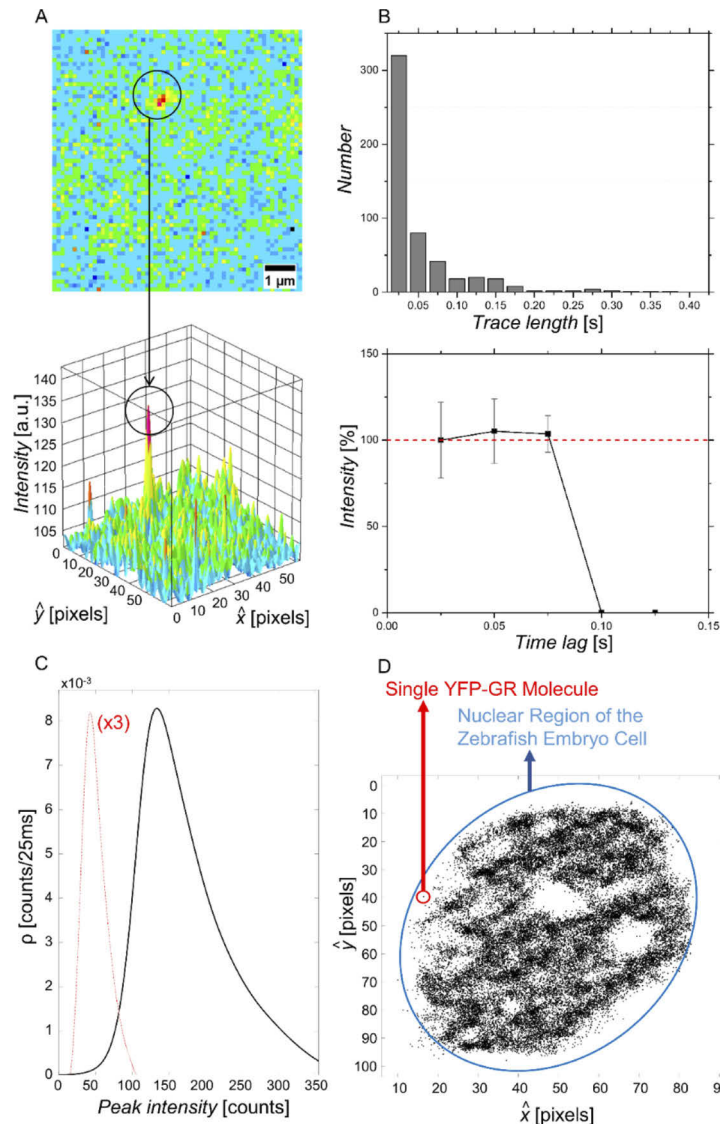


**Fig. 3.** Characterization of detected fluorescence signals from individual YFP-GR molecules in fixed HEK293 cells. (A) Localization of a single fluorescent molecule. The circle indicates a fluorescence intensity spot that was attributed to an individual YFP molecule based on single-step photobleaching. (B) Top: Bar graph depicting the trace length of 1241 single molecules (521 traces) identified in images of fixed HEK293 cells. The average trace lengths equaled 2.3 frames, and approximately 85% of all traces consisted of 1-3 frames. Bottom: Time trace of the relative single-molecule fluorescence signals determined for all YFP-GR molecules showing a trace length of 1-3 frames. All traces show single-step photobleaching indicating that the signals can indeed be attributed to single YFP-GR molecules. (C) Density ( $\rho$ ) plot representing the distribution of the peak intensity of 1241 fluorescence signals. The curve is nearly Gaussian-shaped with a maximum of 139.8 counts per 25 ms, corresponding to 22.3 photons. The signal intensity of the background is shown for comparison (dashed red line, density values are multiplied by 3 for better visualization) (D) Localization of single YFP-GR molecules in the nucleus of a nucleus in a living zebrafish embryo. The image depicts a representative localization of YFP-GR molecules, with an average of  $19.6 \pm 8.7$  peaks per frame, accumulated from 3000 consecutive frames. Nucleoli are visible (white circular regions inside of the nucleus), in which YFP-GR molecules are not found.

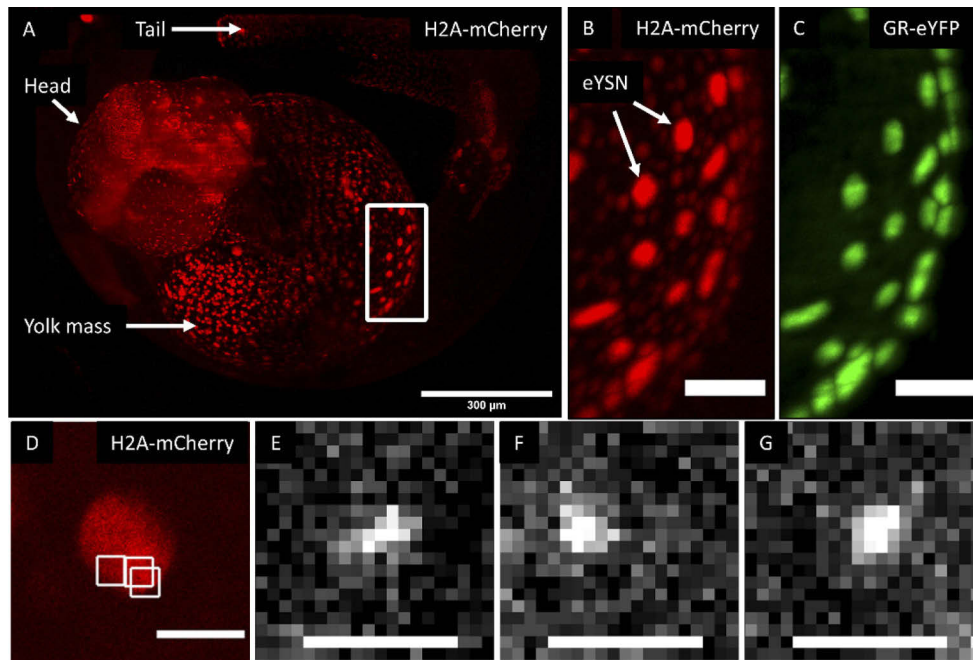


**Fig. 4.** Imaging of YFP-GR in a zebrafish embryo. (A) Maximum intensity projection of a z-stack obtained using LSFM imaging of a developing 1 dpf Tg(actb2:mCherry-H2A) zebrafish embryo injected with a YFP-GR expression vector (only H2A signal shown in A). Scale bar 300  $\mu$ m. (B/C). Higher magnification image of the highlighted ROI showing the (B) mCherry-H2A and (C) the YFP-GR signal (maximum intensity projections, scale bars 50  $\mu$ m). Imaging performed using a different LSFM setup. The expression of GR is evident, as well as the localization within the eYSN. (D) Image of a nuclei in the yolk from a 2 dpf live zebrafish embryo obtained using the LSFMM setup. Only H2A signal shown, scale bar 10  $\mu$ m. (E-G) Three individual YFP-GR molecules imaged through the LSFMM setup within the ROIs highlighted in D (white squares), in a 2 dpf zebrafish embryo. Scale bars 2  $\mu$ m.

To study the effect of GR activation, embryos were imaged in the absence and presence of the synthetic glucocorticoid dexamethasone. One zebrafish embryo was selected for both vehicle- and dexamethasone-treated groups, and in each of the selected embryos three separate areas were imaged. Images exhibited the presence of fluorescence intensity peaks, which were then attributed to single molecules. A projection of 1000-4000 consecutive frames (as shown in Fig. 3(D)) showed a different density of fluorescence intensity peaks between the nucleus and the cytoplasm and served as a matrix for selecting the area of studying protein mobility patterns, so only localizations of nuclear GRs were taken into consideration. Resulting average density of GR molecules per image equaled  $19.6 \pm 8.7$ . A representative image depicting nuclear GRs localization is presented in [Supplement 1, Fig. S3](#).

To determine the mobility pattern of the molecules, the particle image correlation spectroscopy (PICS) analysis was used, which in contrast to other methods that are based on tracking of molecules, requires no a priori knowledge about the dynamical coefficients and works in principle for arbitrarily large molecule densities [36]. In PICS analysis, positions of single YFP-GR molecules between all consecutive image pairs are correlated. After elimination of random correlations, differences in molecular positions between subsequent images resulting from movement of individual molecules (i.e. squared displacements) remained. The latter were plotted in a cumulative distribution plot and fitted to a biexponential probability function, which

indicated the presence of two subpopulations: a fast and a slow subpopulation based on their differing mean squared displacements (MSDs) (Fig. 5(A)). Next, values of subpopulation sizes and MSDs for the fast and slow subpopulations were determined and plotted for each of the selected time lags (i.e., 25, 50, 75, 100, and 125 ms). The resulting plot, depicting the size of the fast population  $\alpha$ , showed that this parameter remained stable across time lags (Fig. 5(B)). The plots depicting MSD function of time for both the fast (Fig. 5(C)) and the slow (Fig. 5(D)) subpopulation showed curves that reached a plateau at larger time lags. Therefore, we fitted these MSDs curves using a confined diffusion model, in which the molecules diffuse freely with an initial diffusion coefficient  $D_0$  and are confined to an area described by a square with a side length  $L$ . Analogous analysis was performed in the fixed HEK293 cells data for comparison, results of which can be found in the Supplement 1, Fig. S1. This analysis showed the predominant presence of one fraction ( $94.8 \pm 1.3\%$ ) with the diffusion coefficient of  $0.041 \pm 0.038 \mu\text{m}^2 \text{s}^{-1}$ . Evident immobility of this fraction obtained for the fixed YFP-GR molecules signifies that the PICS software is a suitable tool for diffusion analyses in both mobile and immobile molecular fractions.

The results of this analysis exhibited that, in the absence of dexamethasone, the size of the fast subpopulation equaled  $90.4 \pm 1.0\%$ . Treatment with dexamethasone did not result in a significant change in the size of the fast subpopulation ( $77.7 \pm 0.9\%$ ) (Fig. 5(B), Table 1). The initial diffusion coefficient ( $D_0$ ) of the fast subpopulation was  $7.90 \pm 0.53 \mu\text{m}^2 \text{s}^{-1}$  in vehicle-treated embryos. Treatment with dexamethasone significantly lowered this coefficient ( $3.52 \pm 0.12 \mu\text{m}^2 \text{s}^{-1}$ ). Similarly, the size of confinement area ( $L$ ) of the fast subpopulation differed significantly between the vehicle- ( $1233 \pm 7 \text{ nm}$ ) and the dexamethasone-treated ( $912 \pm 5 \text{ nm}$ ) embryos (Fig. 5(C), Table 1).

**Table 1. Results of the analysis of the mobility pattern of YFP-GR in zebrafish embryos.**

Parameter	Vehicle-treated	Dexamethasone-treated
$\alpha$ [%]	$90.4 \pm 1.0$	$77.7 \pm 0.9$
$D_0$ fast subpopulation [ $\mu\text{m}^2 \text{s}^{-1}$ ]	$7.90 \pm 0.53$	$3.52 \pm 0.12$
$D_0$ slow subpopulation [ $\mu\text{m}^2 \text{s}^{-1}$ ]	$0.78 \pm 0.18$	$0.61 \pm 0.13$
$L$ fast subpopulation [nm]	$1233 \pm 7$	$912 \pm 5$
$L$ slow subpopulation [nm]	$322 \pm 4$	$373 \pm 9$

Corresponding  $D_0$  values in the slow subpopulations were lower when compared to their fast counterpart, and equaled  $0.78 \pm 0.18 \mu\text{m}^2 \text{s}^{-1}$  for the vehicle- and  $0.61 \pm 0.13 \mu\text{m}^2 \text{s}^{-1}$  for the dexamethasone-treated group. These values were not affected by dexamethasone treatment. Small sizes of the confinement areas, were observed for the slow subpopulations ( $322 \pm 4 \text{ nm}$  in the vehicle-, and  $373 \pm 9 \text{ nm}$  in the dexamethasone-treated group). They were three- to four-fold lower than the confinement areas observed in the fast subpopulation (Fig. 5(D)).

Finally, we characterized the patterns of variability to determine the main sources of variation during the experiments. First, we analysed the correlations between the number of molecules per image and the parameters describing the mobility pattern (size of the fast subpopulation and MSDs for fast and slow subpopulations, obtained experimentally for the time lag of 25 ms). The results of this analysis showed that there was no correlation between the number of molecules and any of these parameters (correlation coefficients equaled 0.14, 0.46, and 0.22 respectively), indicating that the measured parameters were independent from the density of detected molecules in the FoV.

Subsequently, we used a linear mixed model approach to estimate the variance components within our data, and to determine the sources of the measurement error. In this analysis, we also

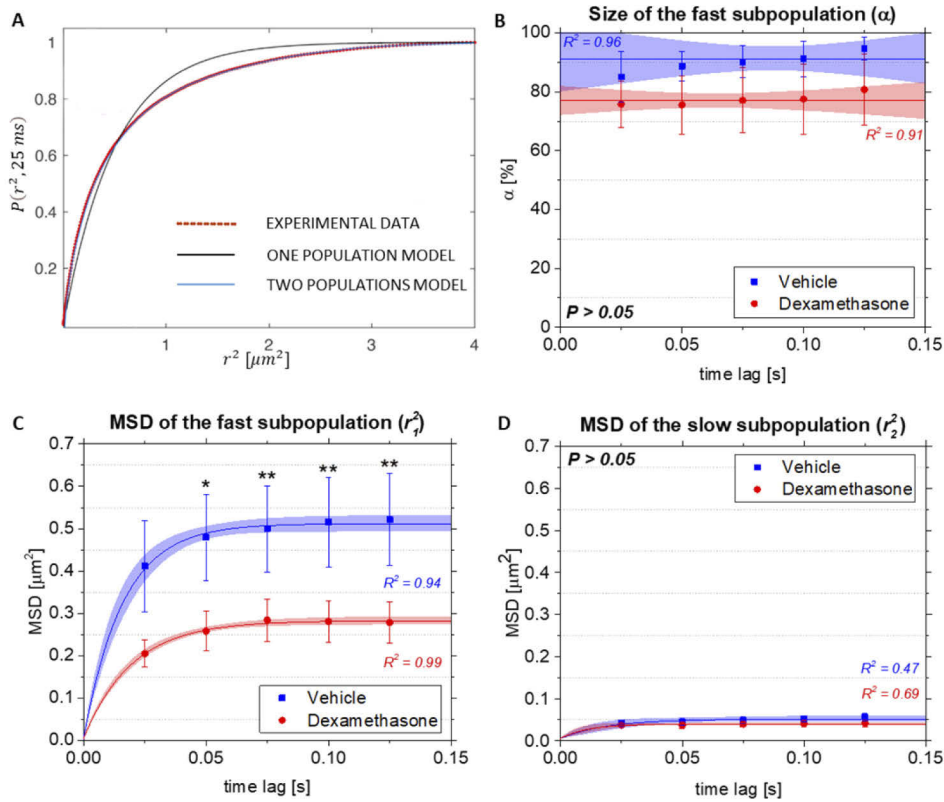


**Fig. 5.** Analysis of the mobility pattern of YFP-GR in zebrafish embryos. Data obtained from three embryos from both the vehicle- (red) and dexamethasone-treated (blue) groups were pooled, and their averages with standard deviations are presented. (A) Cumulative probability  $P$  plot of squared displacement measurements  $r^2$ , obtained experimentally for a time lag of 25 ms. Experimental data are best fitted using a two-population model, yielding the size of the fast subpopulation and the MSD for each time lag. Number of MSD replicates per time lag in each of the groups equaled to 30. (B) Fast subpopulation fraction size in the vehicle- and dexamethasone-treated groups, fitted to a linear model with a fixed slope.  $P(t = 25 \text{ ms})$ : 0.72,  $P(t = 50 \text{ ms})$ : 0.49,  $P(t = 75 \text{ ms})$ : 0.69,  $P(t = 100 \text{ ms})$ : 0.92,  $P(t = 125 \text{ ms})$ : 0.81. The 95% confidence interval and the standard deviation are shown. (C) MSD values for the fast subpopulation for the vehicle- and dexamethasone-treated groups, fitted using a confined diffusion model. The 95% confidence interval and the standard deviation are shown.  $P(t = 25 \text{ ms})$ : 0.11,  $P(t = 50 \text{ ms})$ : 0.02,  $P(t = 75 \text{ ms})$ : < 0.01,  $P(t = 100 \text{ ms})$ : < 0.01,  $P(t = 125 \text{ ms})$ : < 0.01. (D) MSD values for the slow subpopulation for the vehicle- and dexamethasone-treated groups, fitted using a confined diffusion model.  $P(t = 25 \text{ ms})$ : 0.15,  $P(t = 50 \text{ ms})$ : 0.83,  $P(t = 75 \text{ ms})$ : 0.24,  $P(t = 100 \text{ ms})$ : 0.27,  $P(t = 125 \text{ ms})$ : 0.42. The 95% confidence interval and the standard deviation are shown. For (B, C, D), Shapiro-Wilk test was performed to check if data is normally distributed. Significance of the results was conducted using a mixed-effect model for comparison of means between two normally distributed groups. Significant differences are indicated by an asterisk (Significance levels:  $P > 0.05$ , non-significant;  $P < 0.05$ , \*;  $P < 0.01$ , \*\*). Pearson's correlation coefficients  $R^2$  of the model fitness are shown.



included residual variance that displays the extent of variability that cannot be explained by our experimental design (See Table 2).

**Table 2. The variance values  $\sigma^2$  per source parameter and their percentage contribution towards the total variance for the given parameter.<sup>a</sup>**

Subscale	Source of variance					
	$\alpha$		MSD fast subpopulation		MSD slow subpopulation	
	$\sigma^2$	%	$\sigma^2$	%	$\sigma^2$	%
<b>Embryo</b>	0.324	24.9	0.109	21.9	0.016	15.5
<b>Area</b>	0.136	10.5	0.194	39.1	0.006	5.9
<b>Image</b>	0.042	3.2	0.061	12.3	0.015	13.8
<b>Residual</b>	0.800	61.4	0.132	26.7	0.069	64.8

<sup>a</sup>Residuals account for variance that cannot be explained by the experimental design.

A quantitative presentation of the variance analysis together with percentage contributions of each source of variation are presented in Table 2. In this table, the contribution is presented of a single embryo (or an experimental day, since one embryo was imaged per day), an area within an embryo, and the consecutive images taken within the same embryo to the overall variability of the size of the fast subpopulation  $\alpha$ , and the MSDs of the fast and slow subpopulations. For all of parameters selected in the statistical design of our data, a high percentage of the variability came from the sources that could not be controlled for during the experimental design (residual variance of 61.4% for fast subpopulation fraction size,  $\alpha$ , 26.7% for MSD of fast subpopulation, 64.8% for MSD of slow subpopulation; see Table 2). If we exclude the contribution of the unexplained variance towards the total data variability, the linear mixed model analysis demonstrated that most of the variability is observed between imaging different embryos (total variance contribution of 24.9% for fast subpopulation size ( $\alpha$ ), 21.9% for MSD of fast and 15.5% of slow subpopulations respectively). Interestingly, imaging of different areas within an individual embryo showed a large contribution to the variance of the MSD of fast subpopulation (39.1%), but had little effect on the variation of the fast subpopulation size (10.5%) and the MSD of the slow subpopulation (5.9%). By contrast, imaging of the same cell area within an embryo contributed less to the overall variability of the results (See Table 2, Fig. S2).

## 4. Discussion

### 4.1. LSFMM setup

Here we have presented our implementation of a custom LSFMM platform that permits imaging at SMM sensitivity not only in cultured cells, but also in larger and more physiologically relevant biological samples, such as living zebrafish embryos. In a previous study, we have used TIRF microscopy to perform SMM in zebrafish embryos, which enabled SMM analysis in the apical membrane of the outer epidermal cell layer of the embryo [8]. Other related techniques, such as HILO microscopy, would have permitted to reach deeper structures inside these cells, e.g. the nuclei, but the FoV of these techniques are inherently limited. Using the LSFMM setup presented in this study, we are able to visualize individual molecules not only at the membrane of the outer cell layers, but also inside cells, and at a relatively large FoV ( $13.5 \times 300 \mu\text{m}$ ). The developed sample mounting system allowed us to easily position specimens in the tight volume between the two objectives, permitting 3D translations and rotations in order to image the areas of interests. The FEP support and the multilayer Impa mounting permits to sustain samples of various sizes, ranging from cultured cells to zebrafish embryos, with minimal optical aberrations.

Compared to LSFM techniques commonly used for SMM studies [14–19], the presented LSFSMM setup features a simpler optical design: in the excitation path, conventional Gaussian beams are employed, which helps also non-expert users in both alignment and experimental procedures. This illumination path also facilitates the sample mounting, as no additional components (such as a prism [14] or micro-mirrors [15–17]) are inserted. Moreover, the iSPIM configuration permits to free the top part of the FEP support, minimizing optical aberrations. Finally, the setup is assembled from commercially available parts. Altogether, this implementation will permit other laboratories to adopt the technique as well to further expand the application of LSFM to the sub-cellular level within living organisms such as zebrafish embryos.

We demonstrated the capability of our LSFSMM platform to image individual molecules inside an intact living organism using zebrafish embryos. Our custom-designed sample support and sample-mounting procedure enabled the conduction of experiments on the same 2dpf zebrafish embryos for several hours, while leaving the embryo in a healthy condition. At the same time this procedure helped in minimizing the optical aberrations due to the mounting medium. After the imaging sessions we always confirmed that the samples had survived the procedure stress-free, as we were able to let them further develop without mortality or obvious malformations. Moreover, in two experiments we performed imaging on a 2dpf zebrafish embryo, kept it overnight in the microscope and continued the experiment the next day. These quality control experiments enabled us to conclude that no phototoxicity or adverse developmental effects were induced in the embryos during the imaging session and ensured the suitability of the developed method.

We therefore believe that our implementation permits innovative SMM studies in which the mobility patterns of the single molecules are analyzed not only at a single time point, but also over prolonged periods of time in the same living individual, which enables investigating the correlation between sub-cellular molecular dynamics and macro-events such as the developmental stage, metabolism, drug induction or cell and tissue differentiation. To perform this kind of experiments, the imaging chamber is also designed to support a temperature control system ensuring ideal environmental conditions for zebrafish development or other living organisms readily mountable using our setup.

#### 4.2. *Glucocorticoid receptor mobility patterns in zebrafish embryos*

In this study, we have used our LSFSMM setup to analyse the dynamics of the GR inside nuclei (in particular the eYSN) in living zebrafish embryos. The results of this analysis show that single YFP-GR molecules can be detected in these nuclei with a positional accuracy of 76 nm and a temporal resolution of 25 ms. The positional accuracy in our study is relatively lower than the values of circa 40 nm, which were reported in previous studies [8,28,29]. The difference is due to the implemented microscopy setup, which incorporated the detection objective of a lower NA (1.0). Analysis of the mobility pattern of the GR inside these nuclei revealed that these molecules can be divided in a fast and a slow diffusing subpopulation. The occurrence of a fast- and a slow-diffusing subpopulation of GR molecules has been observed previously for GR and other transcription factors [29], and has been interpreted as GRs that diffuse freely within the nucleus, and receptors that interact with DNA respectively. In a recent study, it was shown that this fast subpopulation could, in turn, be divided into two fractions with different mobility, of which the fastest one was interpreted as receptors diffusing freely through the nucleus, and the slowest one as GRs interacting non-specifically with the DNA [28]. The biological function and implications of such GR-DNA interactions have been widely discussed in previous studies [15,20,29,47]. As a result of the lower spatial and temporal resolution of the imaging, fitting of the data with a three-population model did not yield consistent results, so in the current research, we could only distinguish two GR subpopulations. Our findings show that the vast majority of the GR molecules belonged to the fast subpopulation, which constituted approximately 90% of the total GR population in the vehicle-, and 77% in the dexamethasone-treated group. This

percentage is remarkably higher than previously reported sizes of this subpopulation, which were between 45 and 60% in the nuclei of cultured cells upon activation by cortisol or dexamethasone [15,28,29,48]. The difference between our control-treated zebrafish embryos and previously reported cortisol-treated cellular models, might be explained by a lack of a properly developed cortisol secretion in 2 dpf embryos [49], but this does not entirely explain the differences between these models upon dexamethasone treatment. The high percentage of fast-diffusing molecules is better explained by the large size of the eYSN. A larger fraction of freely-diffusing GRs may be expected with more nuclear space available and the same amount of chromatin present.

Interestingly, GR molecules in either of the subpopulations did not move within the entire nuclear environment, but were confined to areas with a size of around 1233 nm for the fast subpopulation and 322 nm for the slow subpopulation (which is so close to the spatial resolution of our setup that this subpopulation might as well be considered immobile). The confinement of the GRs has not been observed in previous studies on the receptor mobility patterns. In our approach, however, we were able to reconstruct the square displacements of GRs in both fractions over a longer period of time, to determine the occurrence of nuclear areas beyond which the diffusion of the GRs is restricted. Such a confinement of the fast GR subpopulation indicates that the receptors diffuse within areas surrounded by barriers, which in the nucleus could be formed by chromatin.

The (initial) diffusion coefficients of the two subpopulations equaled  $7.90 \pm 0.53 \mu\text{m}^2 \text{s}^{-1}$  for the fast subpopulation, and  $0.78 \pm 0.18 \mu\text{m}^2 \text{s}^{-1}$  for the slow subpopulation. Previous studies reported on values of the GR fast fraction diffusion coefficients to fall within the range of circa 2.5 and  $9 \mu\text{m}^2 \text{s}^{-1}$  [15,28,29], which was also observed for other transcription factors, such as p53 or STAT1 [50,51]. We conclude that the values for the diffusion coefficients that were obtained in our approach fall well within the previously published range. The slow subpopulation was characterized by a tenfold lower diffusion coefficient. Studies performed on cellular models report that these coefficients for the GR slow subpopulation to fall within the range between 0.03 and  $0.50 \mu\text{m}^2 \text{s}^{-1}$  [15,28,29].

#### 4.3. *Effect of dexamethasone treatment on the mobility patterns of the glucocorticoid receptor subpopulations*

In the present study, we found that treating zebrafish embryos with dexamethasone for 3 hours prior to the imaging did not significantly alter the size of the subpopulation of GRs. However, in previous studies it has consistently been shown that dexamethasone, as a high-affinity GR agonist, decreases the size of the fast subpopulation, which is generally believed to reflect a larger fraction of GRs interacting with DNA in order to modulate the transcription of genes [29]. We may have failed to detect a significant decrease in population size due to a limited resolution of our experimental approach, but alternatively, the lack of a dexamethasone effect on the population size in our study may be due to the specific characteristics of the eYSN.

In addition, we show that treatment with dexamethasone leads to a smaller confinement area (912 nm) for the fast GR subpopulation. The smaller size of the confinement area for the fast GR subpopulation of the dexamethasone-treated group may be explained by the dexamethasone-activated GR molecules constituting a part of larger multi-protein complexes. These complexes, containing multiple receptor molecules and transcriptional coregulatory proteins, are present inside the cell nucleus and participate in transcription of GR target genes. Diffusion of the GR molecules in such bulky multi-protein aggregates might, therefore, be limited, resulting in the smaller confinement areas in the dexamethasone-treated groups.

Treatment with dexamethasone also resulted in a decrease of the diffusion coefficient from 7.90 to  $3.52 \mu\text{m}^2 \text{s}^{-1}$  in the fast subpopulation, and from 0.78 to  $0.61 \mu\text{m}^2 \text{s}^{-1}$  in the slow one. In a previous study conducted on cultured cells, activation with a high affinity ligand such as dexamethasone resulted in lower diffusion coefficients of the mobile fraction as well, although

a smaller effect was observed [29]. Lower diffusion coefficients of the mobile fraction might also point to a previously described slow-diffusion state, in which GR-ligand molecules bind non-specifically to the DNA in search of their proper binding site [28]. Our results, therefore, confirm the findings established in cellular models that the interactions between ligand and receptor determine GR-DNA binding events.

It must be pointed out that the exposure time ( $T$ ) used in our experiments (0.025 s) is relatively long compared to the diffusion coefficient ( $D_0$ ) and size of confinement area ( $L$ ) of the molecules under investigation. Due to motion blur, this may result in incorrect determination of the parameters  $L$  and  $D_0$ . However, a set of formulas,  $L^2/12D_0 \geq 2T/3$ , proposed by Destainville and Salomé [52], can be used to calculate the accurate values from the experimentally determined ones. Using this method, which was recently validated by Mortensen et al. [53], we determined confinement sizes of 1872 and 1236 nm for the vehicle- and dexamethasone-treated groups, respectively, and diffusion coefficients of 37.9 and 11.1  $\mu\text{m}^2 \text{s}^{-1}$ . These latter values are surprisingly high, especially compared to previous results obtained in cultured cells [15,28,29], and in future studies we would like to attempt confirming these remarkably high diffusion rates of GRs in eYSN of zebrafish embryos.

#### 4.4. Variability of the glucocorticoid receptor mobility patterns

Finally, we analysed the sources of variation in these experiments. This analysis revealed that most of the existing variability in *in vivo* protein mobility measurements originated from imaging different embryos as well as imaging different cell areas within an individual embryo. However, while imaging different embryos constituted a major component of the data variability for all parameters measured (from 15.5% of the total variability for slow population MSD till 24.9% for the size of the fast population, see Table 2), imaging different cell areas was a major component only in the case of the fast population MSD (39.1% of the total variability). We suggest that the differences in values of the parameters between individual embryos might stem from an inherent genetic variation between different zebrafish batches. The absence of inbred zebrafish strains and resulting increased genetic variability is a factor that probably contributed to the overall variability of the GR mobility patterns. As imaging different cell areas within an individual embryo leads to an increase in variability of the fast subpopulation MSD only, it is likely that the architecture of the nucleus hinders the displacement of the fast-diffusing GRs in a cell-dependent manner. Specific nuclear chromatin organization might have led to the increase in observed differences in the MSD values of the fast subpopulation between individual nuclei of embryonic cells.

**Funding.** Ministerio de Economía y Competitividad (RYC-2015-17935, CEX2019-000910-S); Fundación Cellex (Mir-Puig); Laserlab-Europe (871124); Generalitat de Catalunya (CERCA); Fundación Cellex; Horizon 2020 Framework Programme (721537).

**Acknowledgments.** We thank Dr. Verena Ruprecht from the Centre for Genomic Regulation (CRG, Barcelona) for the Tg(actb2:mCherry-H2A) embryos, Prof. Dr. Thomas Schmidt (Leiden University) for support with the analysis of the GR mobility pattern, Dr. Maria Marsal and Dr. Jordi Andilla (ICFO, Barcelona) for scientific advice and logistic assistance. MB and RJG are supported from funding from the European Union's Horizon 2020 research and innovation programme under the Marie Skłodowska-Curie grant agreement ImageInLife (No 721537). We acknowledge financial support from the Spanish Ministry of Economy and Competitiveness through the "Severo Ochoa" program for Centres of Excellence in R&D (CEX2019-000910-S), from Fundació Privada Cellex, Fundació Mir-Puig, Generalitat de Catalunya through the CERCA program and Laserlab-Europe EU-H2020 (871124). EJG acknowledges MINECO/FEDER Ramón y Cajal program (RYC-2015-17935).

MB, RJG, MJMS and PLA designed the experiments. MB and RJG conducted the experiments. MB, GCO, and EJG built the microscopes and implemented the acquisition software. MB developed the sample mounting system, RJG conducted the single molecule analysis, PvH conducted the data statistical analysis. MB and RJG wrote the manuscript, all authors reviewed and edited the manuscript. EJG, MJMS and PLA supervised the work.

**Disclosures.** The authors declare no conflict of interests.

**Data availability.** Data underlying the results presented in this paper are not publicly available at this time but may be obtained from the authors upon reasonable request

**Supplemental document.** See [Supplement 1](#) for supporting content.

## References

1. H. Yokota, "Fluorescence microscopy for visualizing single-molecule protein dynamics," *Biochim. Biophys. Acta, Gen. Subj.* **1864**(2), 129362 (2020).
2. G. S. Harms, L. Cognet, P. H. Lommerse, G. A. Blab, and T. Schmidt, "Autofluorescent proteins in single-molecule research: applications to live cell imaging microscopy," *Biophys. J.* **80**(5), 2396–2408 (2001).
3. R. Iino, I. Koyama, and A. Kusumi, "Single molecule imaging of green fluorescent proteins in living cells: E-cadherin forms oligomers on the free cell surface," *Biophys. J.* **80**(6), 2667–2677 (2001).
4. F. Luo, G. Qin, T. Xia, and X. Fang, "Single-molecule imaging of protein interactions and dynamics," *Annu. Rev. Anal. Chem.* **13**(1), 337–361 (2020).
5. H. Li and J. C. Vaughan, "Switchable fluorophores for single-molecule localization microscopy," *Chem. Rev.* **118**(18), 9412–9454 (2018).
6. D. Axelrod, "Total internal reflection fluorescence microscopy in cell biology," *Traffic* **2**(11), 764–774 (2001).
7. M. Tokunaga, N. Imamoto, and K. Sakata-Sogawa, "Highly inclined thin illumination enables clear single-molecule imaging in cells," *Nat. Methods* **5**(2), 159–161 (2008).
8. M. J. M. Schaaf, W. J. A. Koopmans, T. Meckel, J. van Noort, B. E. Snaar-Jagalska, T. S. Schmidt, and H. P. Spaijk, "Single-molecule microscopy reveals membrane microdomain organization of cells in a living vertebrate," *Biophys. J.* **97**(4), 1206–1214 (2009).
9. O. E. Olarte, J. Andilla, E. J. Gualda, and P. Loza-Alvarez, "Light-sheet microscopy: a tutorial," *Adv. Opt. Photonics* **10**(1), 111–179 (2018).
10. J. G. Ritter, R. Veith, J.-P. Siebrasse, and U. Kubitscheck, "High-contrast single-particle tracking by selective focal plane illumination microscopy," *Opt. Express* **16**(10), 7142–7152 (2008).
11. J.-H. Spille, T. Kaminski, H.-P. Königshoven, and U. Kubitscheck, "Dynamic three-dimensional tracking of single fluorescent nanoparticles deep inside living tissue," *Opt. Express* **20**(18), 19697–19707 (2012).
12. B. Yu, J. Yu, W. Li, B. Cao, H. Li, D. Chen, and H. Niu, "Nanoscale three-dimensional single particle tracking by light-sheet-based double-helix point spread function microscopy," *Appl. Opt.* **55**(3), 449–453 (2016).
13. J. G. Ritter, R. Veith, A. Veenendaal, J. P. Siebrasse, and U. Kubitscheck, "Light sheet microscopy for single molecule tracking in living tissue," *PLoS One* **5**(7), e11639 (2010).
14. Y. Li, Y. Hu, and H. Cang, "Light sheet microscopy for tracking single molecules on the apical surface of living cells," *J. Phys. Chem. B* **117**(49), 15503–15511 (2013).
15. J. C. M. Gebhardt, D. M. Suter, R. Roy, Z. W. Zhao, A. R. Chapman, S. Basu, T. Maniatis, and X. S. Xie, "Single-molecule imaging of transcription factor binding to DNA in live mammalian cells," *Nat. Methods* **10**(5), 421–426 (2013).
16. F. Greiss, M. Deligiannaki, C. Jung, U. Gaul, and D. Braun, "Single-molecule imaging in living drosophila embryos with reflected light-sheet microscopy," *Biophys. J.* **110**(4), 939–946 (2016).
17. M. Reisser, A. Palmer, A. P. Popp, C. Jahn, G. Weidinger, and J. C. M. Gebhardt, "Single-molecule imaging correlates decreasing nuclear volume with increasing TF-chromatin associations during zebrafish development," *Nat. Commun.* **9**(1), 5218 (2018).
18. L. Gao, L. Shao, C. D. Higgins, J. S. Poulton, M. Peifer, M. W. Davidson, X. Wu, B. Goldstein, and E. Betzig, "Noninvasive imaging beyond the diffraction limit of 3D dynamics in thickly fluorescent specimens," *Cell* **151**(6), 1370–1385 (2012).
19. B.-C. Chen, W. R. Legant, K. Wang, L. Shao, D. E. Milkie, M. W. Davidson, C. Janetopoulos, X. S. Wu, J. A. Hammer III, Z. Liu, B. P. English, Y. Mimori-Kiyosue, D. P. Romero, A. T. Ritter, J. Lippincott-Schwartz, L. Fritz-Laylin, R. D. Mullins, D. M. Mitchell, J. N. Bembenek, A.-C. Reymann, R. Böhme, S. W. Grill, J. T. Wang, G. Seydoux, U. S. Tulu, D. P. Kiehart, and E. Betzig, "Lattice light-sheet microscopy: imaging molecules to embryos at high spatiotemporal resolution," *Science* **346**(6208), 1257998 (2014).
20. J. Chen, Z. Zhang, L. Li, B.-C. Chen, A. Revyakin, B. Hajji, W. Legant, M. Dahan, T. Lionnet, E. Betzig, R. Tjian, and Z. Liu, "Single-molecule dynamics of enhanceosome assembly in embryonic stem cells," *Cell* **156**(6), 1274–1285 (2014).
21. Z. Liu, W. R. Legant, B.-C. Chen, L. Li, J. B. Grimm, L. D. Lavis, E. Betzig, and R. Tjian, "3D imaging of Sox2 enhancer clusters in embryonic stem cells," *Elife* **3**, e04236 (2014).
22. F. Aguet, S. Upadhyayula, R. Gaudin, Y.-Y. Chou, E. Cocucci, K. He, B.-C. Chen, K. Mosaliganti, M. Pasham, W. Skillern, W. R. Legant, T.-L. Liu, G. Findlay, E. Marino, G. Danuser, S. Megason, E. Betzig, and T. Kirchhausen, "Membrane dynamics of dividing cells imaged by lattice light-sheet microscopy," *Mol. Biol. Cell* **27**(22), 3418–3435 (2016).
23. M. Mir, A. Reimer, J. E. Haines, X.-Y. Li, M. Stadler, H. Garcia, M. B. Eisen, and X. Darzacq, "Dense Bicoid hubs accentuate binding along the morphogen gradient," *Genes Dev.* **31**(17), 1784–1794 (2017).
24. M. Mir, A. Reimer, M. Stadler, A. Tangara, A. S. Hansen, D. Hockemeyer, M. B. Eisen, H. Garcia, and X. Darzacq, "Single molecule imaging in live embryos using lattice light-sheet microscopy," *Methods Mol. Biol.* **1814**, 541–559 (2018).

25. Y. Wu, A. Ghitani, R. Christensen, A. Santella, Z. Du, G. Rondeau, Z. Bao, D. Colón-Ramos, and H. Shroff, "Inverted selective plane illumination microscopy (iSPIM) enables coupled cell identity lineaging and neurodevelopmental imaging in *Caenorhabditis elegans*," *Proc. Natl. Acad. Sci. U. S. A.* **108**(43), 17708–17713 (2011).
26. H. W. Detrich III, M. Westerfield, and L. I. Zon, "Overview of the zebrafish system," *Methods Cell Biol.* **59**, 3–10 (1998).
27. D. Y. Stainier, B. Fouquet, J. N. Chen, K. S. Warren, B. M. Weinstein, S. E. Meiler, M. A. Mohideen, S. C. Neuhaus, L. Solnica-Krezel, A. F. Schier, F. Zwartkruis, D. L. Stemple, J. Malicki, W. Driever, and M. C. Fishman, "Mutations affecting the formation and function of the cardiovascular system in the zebrafish embryo," *Development* **123**(1), 285–292 (1996).
28. V. I. P. Keizer, S. Coppola, A. B. Houtsmuller, B. Geverts, M. E. van Royen, T. Schmidt, and M. J. M. Schaaf, "Repetitive switching between DNA-binding modes enables target finding by the glucocorticoid receptor," *J. Cell Sci.* **132**(5), jcs217455 (2019).
29. F. L. Groeneweg, M. E. van Royen, S. Fenz, V. I. P. Keizer, B. Geverts, J. Prins, E. R. de Kloet, A. B. Houtsmuller, T. S. Schmidt, and M. J. M. Schaaf, "Quantitation of glucocorticoid receptor DNA-binding dynamics by single-molecule microscopy and FRAP," *PLoS One* **9**(3), e90532 (2014).
30. D. A. Garcia, G. Fettweis, D. M. Presman, V. Paakinaho, C. Jarzynski, A. Upadhyaya, and G. L. Hager, "Power-law behavior of transcription factor dynamics at the single-molecule level implies a continuum affinity model," *Nucleic Acids Res.* **49**(12), 6605–6620 (2021).
31. V. Paakinaho, D. M. Presman, D. A. Ball, T. A. Johnson, R. L. Schiltz, P. Levitt, D. Mazza, T. Morisaki, T. S. Karpova, and G. L. Hager, "Single-molecule analysis of steroid receptor and cofactor action in living cells," *Nat. Commun.* **8**(1), 15896 (2017).
32. M. J. M. Schaaf, A. Chatzopoulou, and H. P. Spaink, "The zebrafish as a model system for glucocorticoid receptor research," *Comp. Biochem. Physiol., Part A: Mol. Integr. Physiol.* **153**(1), 75–82 (2009).
33. J. Schindelin, I. Arganda-Carreras, E. Frise, V. Kaynig, M. Longair, T. Pietzsch, S. Preibisch, C. Rueden, S. Saalfeld, B. Schmid, J.-Y. Tinevez, D. J. White, V. Hartenstein, K. Eliceiri, P. Tomancak, and A. Cardona, "Fiji: an open-source platform for biological-image analysis," *Nat. Methods* **9**(7), 676–682 (2012).
34. T. Schmidt, G. J. Schütz, W. Baumgartner, H. J. Gruber, and H. Schindler, "Imaging of single molecule diffusion," *Proc. Natl. Acad. Sci. U. S. A.* **93**(7), 2926–2929 (1996).
35. U. Krzic, S. Gunther, T. E. Saunders, S. J. Streichan, and L. Hufnagel, "Multiview light-sheet microscope for rapid in toto imaging," *Nat. Methods* **9**(7), 730–733 (2012).
36. S. Semrau and T. Schmidt, "Particle image correlation spectroscopy (PICS): retrieving nanometer-scale correlations from high-density single-molecule position data," *Biophys. J.* **92**(2), 613–621 (2007).
37. G. J. Schütz, H. Schindler, and T. Schmidt, "Single-molecule microscopy on model membranes reveals anomalous diffusion," *Biophys. J.* **73**(2), 1073–1080 (1997).
38. D. Bates, M. Mächler, B. Bolker, and S. Walker, "Fitting linear mixed-effects models using lme4," *J. Stat. Software* **67**(1), 1–48 (2015).
39. S. G. Luke, "Evaluating significance in linear mixed-effects models in R," *Behav. Res. Methods* **49**(4), 1494–1502 (2017).
40. P. H. M. Lommerse, G. A. Blab, L. Cognet, G. S. Harms, B. E. Snaar-Jagalska, H. P. Spaink, and T. Schmidt, "Single-molecule imaging of the H-ras membrane-anchor reveals domains in the cytoplasmic leaflet of the cell membrane," *Biophys. J.* **86**(1), 609–616 (2004).
41. N. Bobroff, "Position measurement with a resolution and noise-limited instrument," *Rev. Sci. Instrum.* **57**(6), 1152–1157 (1986).
42. C. B. Kimmel and R. D. Law, "Cell lineage of zebrafish blastomeres. II. Formation of the yolk syncytial layer," *Dev. Biol.* **108**(1), 86–93 (1985).
43. C. B. Kimmel, W. W. Ballard, S. R. Kimmel, B. Ullmann, and T. F. Schilling, "Stages of embryonic development of the zebrafish," *Dev. Dyn. an Off. Publ. Am. Assoc. Anat.* **203**(3), 253–310 (1995).
44. L. Carvalho and C.-P. Heisenberg, "The yolk syncytial layer in early zebrafish development," *Trends Cell Biol.* **20**(10), 586–592 (2010).
45. L.-T. Chu, S. H. Fong, I. Kondrychyn, S. L. Loh, Z. Ye, and V. Korzh, "Yolk syncytial layer formation is a failure of cytokinesis mediated by Rock1 function in the early zebrafish embryo," *Biol. Open* **1**(8), 747–753 (2012).
46. D. W. Williams, F. Müller, F. L. Lavender, L. Orbán, and N. Maclean, "High transgene activity in the yolk syncytial layer affects quantitative transient expression assays in zebrafish (*Danio rerio*) embryos," *Transgenic Res.* **5**(6), 433–442 (1996).
47. M. E. van Royen, S. M. Cunha, M. C. Brink, K. A. Mattern, A. L. Nigg, H. J. Dubbink, P. J. Verschure, J. Trapman, and A. B. Houtsmuller, "Compartmentalization of androgen receptor protein-protein interactions in living cells," *J. Cell Biol.* **177**(1), 63–72 (2007).
48. D. M. Presman, M. F. Ogara, M. Stortz, L. D. Alvarez, J. R. Pooley, R. L. Schiltz, L. Grøntved, T. A. Johnson, P. R. Mittelstadt, J. D. Ashwell, S. Ganesan, G. Burton, V. Levi, G. L. Hager, and A. Pecci, "Live cell imaging unveils multiple domain requirements for in vivo dimerization of the glucocorticoid receptor," *PLoS Biol.* **12**(3), e1001813 (2014).
49. D. Alsop and M. M. Vijayan, "Molecular programming of the corticosteroid stress axis during zebrafish development," *Comp. Biochem. Physiol., Part A: Mol. Integr. Physiol.* **153**(1), 49–54 (2009).

50. D. Mazza, A. Abernathy, N. Golob, T. Morisaki, and J. G. McNally, "A benchmark for chromatin binding measurements in live cells," *Nucleic Acids Res.* **40**(15), e119 (2012).
51. J. Speil, E. Baumgart, J.-P. Siebrasse, R. Veith, U. Vinkemeier, and U. Kubitscheck, "Activated STAT1 transcription factors conduct distinct saltatory movements in the cell nucleus," *Biophys. J.* **101**(11), 2592–2600 (2011).
52. N. Destainville and L. Salomé, "Quantification and correction of systematic errors due to detector time-averaging in single-molecule tracking experiments," *Biophys. J.* **90**(2), L17–9 (2006).
53. K. I. Mortensen, H. Flyvbjerg, and J. N. Pedersen, "Confined Brownian motion tracked with motion blur: estimating diffusion coefficient and size of confining space," *Front. Phys.* **8**, 601 (2021).